PHYSICAL REVIEW APPLIED **17,** 044014 (2022)

Editors' Suggestion

Energy-Harvesting Coil for Circularly Polarized Fields in Magnetic Resonance Imaging

Pavel S. Seregin,[†] Oleg I. Burmistrov,[†] Georgiy A. Solomakha, Egor I. Kretov, Nikita A. Olekhno, and Alexey P. Slobozhanyuk[*]

[1] *School of Physics and Engineering, ITMO University, Saint Petersburg 197101, Russia*

(Received 6 July 2021; revised 6 February 2022; accepted 2 March 2022; published 7 April 2022)

Specialized radio-frequency coils and sensors placed inside a magnetic resonance imaging (MRI) scanner considerably extend its functionality. However, since cable-connected in-bore devices have several disadvantages compared to the wireless ones, the latter are currently under active development. One of the promising concepts in wireless MRI coils is energy harvesting, which relies on converting the energy carried by the radio-frequency MRI field without the need for additional transmitters, similar to common wireless power-transfer solutions. In this paper, we propose a compact harvesting coil design based on the combination of loop and butterfly coils that allows energy harvesting of a circularly polarized field. By performing numerical simulations and experiments with commonly used Siemens Espree and Avanto 1.5 tesla MRI scanners, we demonstrate that the proposed approach is safe, efficient, does not decrease the quality of MRI images, and allows doubling the harvested voltage compared to the setups with linearly polarized fields.

DOI: 10.1103/PhysRevApplied.17.044014

I. INTRODUCTION

Magnetic resonance imaging (MRI) has established itself as one of the key methods in noninvasive medical visualization. To further extend its functionality, different in-bore devices are applied, including various flexible receive-only body-matrix MRI coils and sensors. However, these devices require an additional energy supply, and powering them with wire lines can result in imaging artifacts or patient discomfort [1]. Thus, various wireless alternatives are actively studied, including MRI energy harvesting [2,3], wireless MRI coils [4], wireless power transfer [5–11], and vibration energy harvesting [12]. While wireless power transfer requires the use of additional transmitting coils, the harvesting relies on the conversion of electromagnetic fields that are already present in the region of interest, such as B_1^+ rf field, Fig. 1. Thus, no modifications of the MRI scanner itself are required in the latter case.

Radio-frequency harvesting setups converting electromagnetic energy from the surrounding environment have been demonstrated for applications in global system for mobile communication (GSM) [13,14], radio-frequency identification (RFID) [15], WiFi [16], and long-term evolution (LTE) [17] frequency ranges. For the conventional wireless communication bands, the power density of environment signals ranges from 2 μW/m^2 to 10 mW/m^2 [18,19], which is much lower than in MRI scanners. However, in contrast to such high-frequency applications, there are several differences in the applications of the energy-harvesting concept in MRI: (i) harvesting should work at frequencies of 63 MHz for 1.5 T MRI and 128 MHz for 3 T, which means that the harvesting process takes place in the near-field region, as the MRI bore size is small compared to the MRI working wavelength (the bore is typically around 70 cm in diameter); (ii) MRI scanners generate rf fields as short high-power pulses up to 10 ms long; (iii) there is a large constant magnetic field B_0 present, which requires the use of nonmagnetic materials; (iv) the currents flowing in the harvesting circuit should not distort the magnetic fields B_1^+ and B_0 to prevent a decrease in the image quality; (v) since MRI is a medical visualization method, strict safety requirements should be met, including the *specific absorption rate* (SAR) limit.

The general principles of energy harvesting and its application in MRI are illustrated in Fig. 1. Inside a MRI scanner, a large constant magnetic field B_0 is created. In the process of MRI scanning, additional pulse gradient fields $G_x(t)$, $G_y(t)$, and $G_z(t)$ are created in order to obtain the spatial resolution [20], which have typical values of $10 - 50$ mT/m [20] and produce peak power up to 1 MW [21]. However, creating an effective coil for their conversion is very challenging [3], since a large coil is needed to capture spatial field variations. Additionally, an RF field B_1^+ is created for the excitation of the nuclear

---

[*] a.slobozhanyuk@metalab.ifmo.ru

[†] These two authors contributed equally

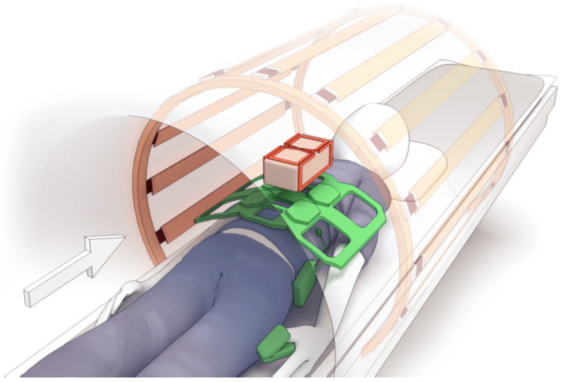

FIG. 1. Scheme of the harvesting setup. The patient located in the MRI scanner (shown in gray) with a large constant magnetic field B_0 (white arrow). The harvesting coil (shown in red) is placed on top of the patient and powers the in-bore devices (shown in green) by converting the energy of the rf field B_1^+. Examples of such in-bore equipment include local coils, heart activity monitors, and pulse sensors.

magnetic resonance at the Larmor frequency [20]. In MRI setups with energy harvesting, a body coil is used for the transmission while a local coil is responsible for the reception of echo signals from protons [22]. We develop RF energy harvesting for MRI with $B_0 \leq 3$ T, since a body coil is not used in ultrahigh field MRI setups [23]. RF field B_1^+ typically has circular polarization and peak pulse power 10–15 kW [24]. Such power is potentially sufficient to provide a dc supply for in-bore electronics, including the circuits of local receive rf coils, electrocardiography (ECG) gating, respiratory sensors (chest movement tracking), pulse sensors (heart rate capturing), or an external triggering source [25]. Moreover, energy-harvesting coils for rf field B_1^+ can be efficiently implemented, as they are compact and do not require multiple-turn design, in contrast to the schemes using gradient coils.

These features have led to several realizations of harvesting setups in MRI [3,26]. However, all of the mentioned setups rely on converting linearly polarized components of B_1^+, which limits the harvesting efficiency due to a circular polarization of the B_1^+ field. In the present paper, we extend the proposed concepts and develop a harvesting coil capable of capturing circularly polarized fields in order to enhance the harvesting efficiency. The paper is organized as follows. In Sec. II, we describe the design of the proposed harvesting coil circuitry. Section III features the results of experimental measurements with the developed harvesting setup performed on MRI machines. In Sec. IV, we perform detailed numerical simulations of the setup in order to evaluate the SAR and estimate the role played by various imperfections. Finally, Sec. V contains concluding remarks. The main text is supplied with Appendices A, B, and C considering the effects of direct currents in the harvesting setup circuitry on the constant magnetic field B_0, details of the experimental setup and characterization of harvesting coil, and energy-harvesting efficiency for different scanning sequences, respectively.

II. COIL DESIGN FOR CIRCULARLY POLARIZED HARVESTING

The proposed harvesting setup design is illustrated in Fig. 2. It includes two coils: the first one with the shape of a loop and the other one being butterfly shaped. The two coils are required to simultaneously convert orthogonal linear parts of the circularly polarized field B_1^+. This is achieved by each coil capturing one linear component. Such a geometry is chosen as it demonstrates the best parameters among the other coil designs compared in Note S1 within the Supplemental Material [27]. The parameters taken into account include (i) the complexity of decoupling circuitry (additional inductors are needed for planar designs realized within a single printed circuit board, while purely geometrical decoupling can be applied for nonplanar designs), (ii) the conversion efficiency, and

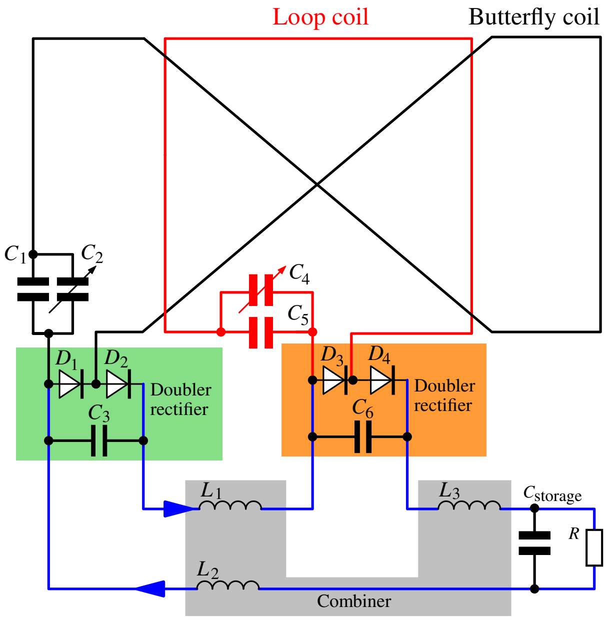

FIG. 2. Schematics of the developed setup for circularly polarized field harvesting. The setup consists of two decoupled coils: one in the form of a circular loop (red solid line) and the other one being butterfly shaped (black solid line). The converted voltage is rectified by two voltage doublers (shaded in green and orange), which include diodes D_1, D_2, D_3, and D_4 along with capacitors C_3 and C_6. The rectified currents are injected in a dc current loop (blue solid lines) where they are added by a combiner consisting of inductors L_1, L_2, and L_3. dc current charges a storage capacitor C_{storage}, from which the power is supplied to a load having the resistance R. Capacitors C_1, C_5 and variable capacitors C_2, C_4 are needed to tune the loop and butterfly coils to their working frequencies.

(iii) the implementation simplicity. The harvesting setup also includes two tuning capacitors C_2 and C_4, one for each coil, which are required to precisely adjust the coil resonance to the Larmor frequency. Then, the currents generated in coils are rectified by voltage doublers to enhance the conversion voltage. Detailed description of the harvesting setup circuitry, including the values and models of all circuit elements, is provided in Appendix A.

The magnitude of output dc current after the rectifiers can reach the values up to 1 A. Thus, the dc part of the harvesting circuit (shown with blue solid lines in Fig. 2) can potentially lead to the emergence of an effective magnetic field disturbing the B_0 field. Since MRI requires an extreme homogeneity of the B_0 field within the imaging volume, such a perturbation can result in considerable imaging artifacts [28]. To eliminate such effects, we use differential pairs for all dc supply lines. Further details are given in Appendix B.

The size of coil elements defines the voltages obtained with the harvesting setup: larger sizes result in larger voltages and higher harvested power, respectively. However, a large harvesting coil may lead to the distortion of the rf field B_1^+ in the vicinity of the coil and decrease the patient's comfort. In the experiments and numerical simulations, we use the following coil parameters: length $L = 110$ mm, width $W = 65$ mm, and height $H = 35$ mm, Fig. 3(a). The brick-shaped substrate is made from extruded polystyrene foam (XPS) covered with a green-colored insulating tape (in order to prevent the foam damage during the soldering of coils and other circuitry). The permittivity of XPS is around $\varepsilon \approx 1.1$ in the frequency range from several kHz to about 1 GHz [29]. Each tuning capacitor is realized as two parallel capacitors: a fixed capacitors C_1 and C_5 and adjustable capacitors C_2 and C_4. The two rectifiers for loop and butterfly coils (orange and green regions in Fig. 2) are realized using Schottky diodes (see Appendix A for further details on the experimental setup).

The rectified currents from the two harvesting coils are combined and charge the storage capacitor, which powers a 500-ohm load R equivalent to the resistance of two Siemens LNA PN 3760688 low-noise amplifiers based on FET transistors that are used in the clinical receive coil arrays. Due to this value of the load, we use a voltage doubler rectifier and the combiner with inductors. However, it should be noted that the overall efficiency depends on the ratio between the equivalent inner resistance of the harvesting system and the resistance of the load, according to the maximum power transfer theorem [30]. Significantly, it is determined by the type of the rectifier: the full bridge is more efficient with a load less than 100 ohm, and a doubler can work more efficiently with a load greater than 100 ohm. The dependence of harvesting voltage on the load resistance is shown in Fig. 3(d).

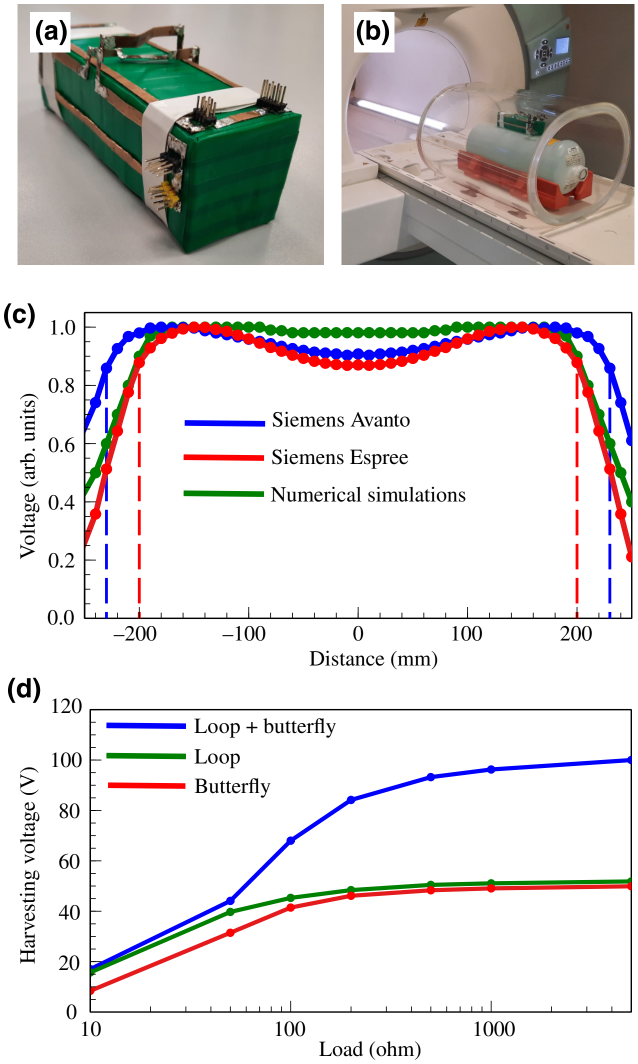

FIG. 3. (a) Photo of the experimentally realized coil for circularly polarized field harvesting. (b) Experimental setup including the MRI scanner, a body phantoms, and the harvesting coil atop of the phantom. (c) Normalized harvesting voltage value relative to the body coil isocenter (z direction) with the harvesting coil located at the height of 1 cm above the phantom. The region between the dashed lines is suitable for harvesting. (d) Harvesting voltage value versus load resistance. The measurements are performed for a doubler rectifier with transmitter adjust voltage manually set to the value $V_{\mathrm{tr}} = 180$ V and the harvesting coil located at the height of 1 cm above the phantom.

To perform experimental studies of the developed harvesting coils with a clinical MRI scanner, we use the following setup illustrated in Fig. 3(b). The harvesting coil is placed atop of a standard MRI Siemens phantom PN 5512608 (used for quality-assurance procedures) having the mass of 7.75 kg and containing distilled water with 1.24 g $(\mathrm{NiSO_4} - 6\mathrm{H_2O}) + 2.62$ g NaCl per 1000 ml of water. The phantom has a diameter of 160 mm and a length of 380 mm (without the filler neck), and is placed in a cylindrical Siemens loaded body phantom PN 5750307 upon the standard pads at the height of 43 mm from its bottom. The loaded body phantom itself is filled with 3 g $(\mathrm{MnCl_2} - 4\mathrm{H_2O}) + 5$ g NaCl per 1000 ml of water. The size of the loaded body phantom is $450 \times 355 \times 525$ mm^3, and the thickness is 15 mm. Both phantoms and the harvesting setup are placed on a patient table, which allows controlling their position inside the MRI scanner.

III. EXPERIMENTAL RESULTS

We start with measuring the output voltage V_{ind} induced at the load R_{load} with rf power applied to the body coil. We study the dependence of the voltage V_{ind} on the distance between the harvesting coil position and the isocenter of the MRI bore magnet z. To change the location of the harvesting coil, we move it manually while keeping the positions of the table and phantom unchanged. Such a procedure is chosen to prevent a change of the transmitting body coil impedance. The output voltage is measured using an Owon XDS3202A 14-bit oscilloscope attached by a coaxial cable with multiple rf traps to avoid the cable antenna effect. We measure the output voltage with a single excitation pulse during transmit, as rf harvesting should provide voltage to the local coil circuitry during each phase-encoding step. To proceed, we apply a manual frequency adjustment procedure employing three separate pulses. However, only the first one is used to measure the output harvesting voltage. The sets of voltage measurements are performed utilizing Siemens Avanto (blue curve) and Siemens Espree (red curve) 1.5 T MRI systems, and numerical simulations with CST Microwave Studio 2020 (green curve). The resulting voltage dependence $V(z)$ is shown in Fig. 3(c). For the numerical model, we use the geometric dimensions equivalent to those of the Siemens Espree body coil. The graphs show that the width of the curves slightly differ because the length of body coils is different. The longer the body coil length is, the larger the working area for harvesting can be obtained. As seen from Fig. 3(c), when the harvesting coil is moved from the isocenter, the voltage first slowly increases, reaching its maximum at $z \approx 14$ cm for the Espree scanner and $z \approx 18$ cm for the Avanto scanner. However, the voltage rapidly drops with a further increase of the distance z, and the harvesting setup becomes inefficient. To estimate the region where the harvesting setup maintains stable functionality, we select a 15% drop in the output voltage as a criterion. Then, as shown by the dashed lines in Fig. 3(c), the realized harvesting coil can be freely moved within ±20 cm range for the Espree setup and within ±22.5 cm range for the Avanto setup without a considerable change in the output voltage. This range is larger than the typical MRI coil size, thus offering a significant degree of freedom in choosing the harvesting coil position. The measurements show that the output voltage can be almost doubled at the harvesting output with a circularly polarized rf coil. Still, the overall efficiency depends on the value of the load.

Next, we study the rf field B_1^+ inside the body phantom for different locations of the harvesting coil to ensure that it does not impact the MRI functionality. The axial cross section of the B_1^+ field in the x-y plane at the isocenter $z = 0$ for the Espree MRI scanner with a body phantom is shown in Fig. 4(b). In the case of Fig. 4(b), no harvesting setup is present, and the magnetic field is nearly homogeneous up to a certain value of noise, which is caused mostly by the pulse sequence chosen for B_1^+ measurement within the applied technique [31]. Then, if the harvesting coil is placed close to the phantom's surface at the distance of 2 cm, the field B_1^+ considerably changes, Fig. 4(c). In particular, the presence of coil leads to the emergence of inhomogeneity on the right side of the phantom. The field pattern becomes asymmetric due to several reasons, including the absence of mirror symmetry of the harvesting coil itself, since the tuning capacitors and rectifiers are introduced in a nonsymmetric fashion. Although the homogeneity is improved in Fig. 4(d) compared to Fig. 4(c) due to the increased distance of 5 cm between the harvesting setup and the phantom, the flip angle (FA) still increases in the presence of the harvester. As the harvesting coil is resonant, it can focus the B_1^+ field near itself. An additional increase in distance can thus significantly improve the homogeneity. This said, the proposed harvesting coil design should not affect the quality of MRI images if placed at a sufficient distance from the patient. Moreover, harvesting voltage for the case when the harvesting coil is located at the height $h = 2$ cm above the phantom is lower than in the case with height $h = 5$ cm by approximately 20%–30% due to the effect of the scanned object placed in the vicinity of harvesting coil, according to the CST Microwave Studio numerical simulations (see Note S3 within the Supplemental Material [27]).

The peak voltage during one rf excitation pulse reaches up to 100 V on the $R = 500$ ohm load. Therefore, the peak power is approximately 21 W. However, the duration of excitation pulses is usually in the range from 100 μs to 5 ms, and repetition time (TR) is typically from 5 ms to several seconds [32]. Besides, the envelope shape of MR (magnetic resonance) signal is not a rectangle, as sinc function is mostly used. As a result, the estimated average power at each step of the phase-encoding cycle is about 100–500 mW.

IV. NUMERICAL SIMULATIONS

To extend our studies, we perform a set of numerical simulations in CST Microwave Studio 2020 (see further details regarding the design of numerical model in Note S3 within the Supplemental Material [27]).

First, we repeat the experimental protocols, starting with the dependence of the harvesting output voltage on the

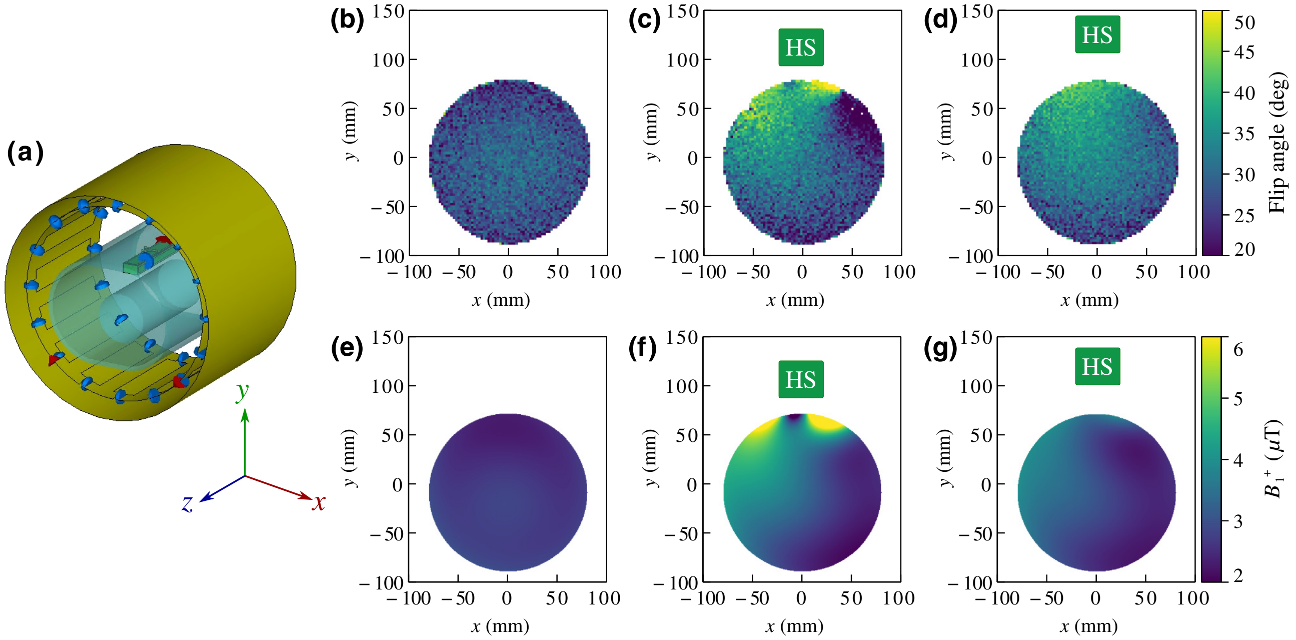

FIG. 4. (a) Numerical model implemented in CST Microwave Studio. The blue cylinder and frame correspond to the water-filled body phantom. The body coil and scanner edge are shown with yellow, while blue disks denote the capacitors placed in the birdcage coil. The harvesting setup (green shaded rectangle with the label HS) is placed atop the phantom and centered at the coordinate origin $x = 0$. Red arrows mark the location of the ports used in numerical simulations. (b)–(g) Maps of the rf magnetic field B_1^+ in the x-y plane for $z = 0$ obtained (b)–(d) experimentally and (e)–(g) numerically for different cases: (b),(e) a single phantom without the harvesting setup, (c),(f) with the harvesting setup located at the height $h = 2$ cm above the phantom, and (d),(g) with the harvesting setup located at the height $h = 5$ cm above the phantom.

distance z shown with the solid green curve in Fig. 3(c). For this simulation, we create a model that includes a birdcage body coil, a homogeneous cylindrical phantom with additional frame resembling the ones used in real experiments, and a detailed model of the harvesting coil, including the necessary lumped elements, Fig. 4(a). As seen from Fig. 3(c), the numerical simulation results agree well with both the Espree and Avanto measurements. However, the numerically obtained voltage values are higher than the experimental ones in the vicinity of the isocenter, by up to 10%, which is likely related to the simplified nature of the model, which does not take into account realistic body coil design features (such as additional slots with serial capacitors) required for eliminating eddy currents.

Then, we calculate the root-mean-square value of the rf field B_1^+ applying the same numerical model in the absence of the harvesting coil, Fig. 4(e), and for the harvesting coil located at different distances from the phantom, Figs. 4(f) and 4(g). As seen from the obtained distributions, the field with the harvesting coil placed at the height of 5 cm closely resembles that in the absence of coil. At the same time, the field is strongly perturbed if the harvesting coil is located at the height of 2 cm. These simulation results fully agree with the experimental findings in Figs. 4(b)–4(d).

The safety of MRI is mostly governed by the SAR, which indicates the amount of rf radiation absorbed by a patient. To verify the patient safety of MRI scanning in the presence of harvesting coil, we evaluate SAR numerically by performing the required simulations in CST Microwave Studio software. The considered MRI harvester is a resonant coil, which does not switch off during the transmission phase. Due to its coupling with the transmit body coil, it can focus rf fields that might cause the appearance of focal spots in SAR. We perform a numerical simulation to estimate the safety issues with a detailed voxel 3D model of a human body (Gustav voxel model), Fig. 5(a). In Fig. 5(b), SAR is calculated without a harvesting coil. The resulting pattern appears asymmetric, with a maximum at one side of the patient. According to the results of numerical simulations with the harvesting coil located at heights of 20 and 50 mm above the voxel model, Figs. 5(c) and 5(d), the local SAR maximum is reduced by 6.8% (0.136 W/kg) and 19.8% (0.117 W/kg), respectively, if compared to the case without harvesting coil (corresponding to the maximal value of 0.146 W/kg). Lower local SAR values can be explained by a change in the field distributions of the body coil in the presence of harvesting setup.

However, local SAR is an unusual quantity for the safety assessment of the clinical MRI scanners. For this purpose, the whole-body SAR values are typically considered. The whole-body SAR is the measure of a total rf power absorbed by the body. In our case, the whole-body SAR

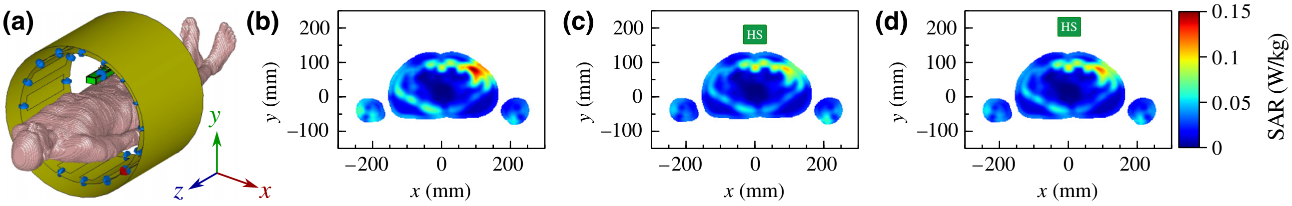

FIG. 5. (a) Voxel human model used for numerical simulations of the SAR. (b)–(d) SAR images in the following cases: (b) without the harvesting setup, (c) with the harvesting setup (green shaded rectangle) placed at the height of 2 cm, and (e) with the harvesting setup placed at the height of 5 cm above the voxel model.

for the harvesting coil located at heights of 20 and 50 mm above the voxel model is lower than in the case without harvesting setup (0.012 W/kg) by 34% (0.0079 W/kg) and 44% (0.0067 W/kg), respectively. These quantities characterize the amount of power dissipated in the voxel model. In the reference case without the harvesting setup, 96% of power is dissipated in the body model. For the cases with harvesting coils placed at 20 and 50 mm, the power dissipated in the body model is 0.67 W (30% lower than in the reference case) and 0.59 W (38.5% lower than in the reference case), respectively. The rest of the power is converted by the harvesting coil or reflected. As a result, the proposed harvesting coil design appears safe for MRI applications. However, lower levels of power absorbed in the voxel model lead to a drop of the B_1^+ field. It is thus worth noting that modern MRI scanners allow compensating this effect via appropriate calibration procedures.

V. CONCLUSION

We develop a design of the energy harvesting coil for MRI applications, which is based on the combination of two decoupled coils. Such a setup allows converting a circularly polarized rf field, in contrast to the previously developed harvesters for linearly polarized fields. Such a modification appears natural, as the field B_1^+ created by the birdcage body coil has a circular polarization. Our experimental studies show that the output voltage of the energy harvesting setup can be almost doubled with a proposed circularly polarized rf coil if compared to conventional harvesting designs. Performing numerical simulations and experimental measurements with clinical MRI scanners, we demonstrate that the proposed harvesting coil design is suitable for low-power consumption devices, meets the patient safety requirements, and does not considerably affect the homogeneity of the rf magnetic field.

The proposed design can be used as a main or additional power supply for multichannel phased array coils, which are the gold standard in clinical MRI imaging. The amount of channels in such coils can reach up to 8 or even higher. At the same time, each channel requires power levels of at least 100–300 mW [5]. Therefore, the power amount of 1–3 W is required for the proper functioning of an eight-channel array, which is now out of the reach of the proposed setup. However, it is possible to implement a wireless phased array coil with one or two channels fully supplied by the proposed harvesting setup. Such coils are used for dental MRI [33]. Besides, the introduced harvester is capable of powering MRI coils with wireless identification and wireless electrocardiographic sensors [34]. The directions for further development of the proposed concept include a detailed consideration of impedance matching between the coils and rectifiers of the harvesting setup, a comparison of different rectifier types (e.g., a combiner based on a 90° hybrid bridge and a single rectifier, etc.), and a direct evaluation of the harvesting setup in combination with local coils and sensors.

ACKNOWLEDGMENTS

This work is supported by the Russian Science Foundation (Project No. 21-79-30038). OB acknowledges RPMA grant of the School of Physics and Engineering of ITMO University. A.S. acknowledges the support by the Foundation for the Advancement of Theoretical Physics and Mathematics “BASIS.”

APPENDIX A: EXPERIMENTAL SETUP AND CHARACTERIZATION OF THE COILS

Since the magnitude of dc current after the rectifiers can reach relatively high values, we use a Vishay Semiconductors VS-10MQ100-M3 Schottky diode in the rectifier as it has a low capacitance of 35 pF for $V_{\mathrm{reverse}} > -10$ V and is capable of working at currents up to 1 A and voltages up to 100 V. It is worth noting that some low-voltage rf Schottky diodes (e.g., Skyworks Solutions SMS-7630-79, Infineon Technologies BAT62, and ON Semiconductor MMBD770T1) may not be suitable for the realization of the proposed harvesting setup due to considerable induced voltages at diodes $D_1 - D_4$, especially for high flip angles. For example, BAT62 diodes broke down during the experimental tests of the first versions of the setup in MRI scanners.

The capacitors C_1 and C_5 (see Fig. 2) are implemented with Johanson Technology S111DUE multilayer high-Q capacitors and have the capacitance

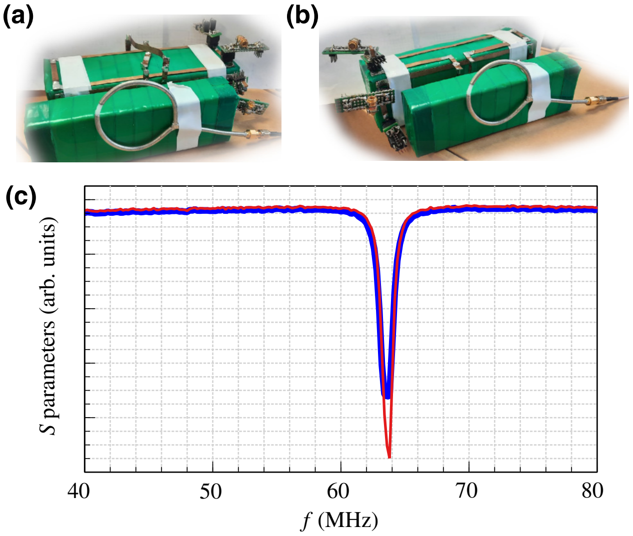

FIG. 6. (a),(b) Photographs of the setups for tuning procedures of (a) the butterfly coil and (b) the loop coil. (c) Measured S_{11} parameters for the butterfly coil (red solid line) and the loop coil (blue solid line) as functions of frequency f .

of 10 pF, the capacitors C_3 and C_6 are KEMET C2220X164KFRLCAUTO with the capacitance of 0.16 μF and the maximum voltage of 1600 V, and the capacitors C_2 and C_4 are Sprague Goodman SGNMA3T20001 with the capacitance of 2–20 pF and the maximum voltage of 1000 V. We prepare custom-made inductors wound with 0.5-mm copper wire with a nominal value of $L_1 = L_2 = L_3 = 6$ μH due to the simplicity of their realization and acceptable loss levels. The inner diameter of coils is 10 mm, and the coil length is 21 mm. It is necessary to note that the tantalum capacitors are not recommended for use in the circuit where high-voltage pulses can be applied. Moreover, it can cause explosions and fire. That is why we use multilayer ceramic capacitors (MLCCs). Finally, the capacitor C_{storage} is Knowles Syfer 2220Y1K00474KXTWS2 having capacitance of 0.47 μF and maximum voltage of 1000 V.

In the experiments, the resonant frequencies of the loop and butterfly coils in the harvesting setup are measured with the help of a field probe and Planar S5048 vector network analyzer. In Fig. 6(a), the setup is placed near the probe in a way to allow the study of the butterfly coil, while in Fig. 6(b) the configuration is set to measure the response of the loop coil. As seen in Fig. 6(c), S_{11} parameters demonstrate a good decoupling of the loop and butterfly coils as the resonant peaks for two orientations of the harvesting setup coincide.

APPENDIX B: EFFECTS OF DC CURRENTS IN THE HARVESTING SETUP ON MAGNETIC FIELD B_0

To address the effects of dc currents in the harvesting setup on the quality of MR images, we use an experimental test bench with a current loop corresponding to the combiner dc circuitry (blue solid line in Fig. 2), which is driven with an external current source GOPHERT NPS-1601. The current is supplied to the current loop via a cable with rf traps placed at a spacing of 20 cm, as if such a current is collected from the coil. The rf traps with a diameter of 3 cm and length of 4 cm are made of coaxial cables with additional tuning capacitors soldered in the cable braid break. The emulating current loop has the shape of a dumbbell with diameters of the round parts being 3 cm and the constriction having a length of 5 cm and a width of 1 cm, respectively, Fig. 7(a). It illustrates the worst possible dc-coil design with the biggest influence on the B_0 field. The static field created by this coil is simulated in CST. The field magnitude is 20 μT for 1-A current at the coil input. To confirm the results of the numerical simulation we perform

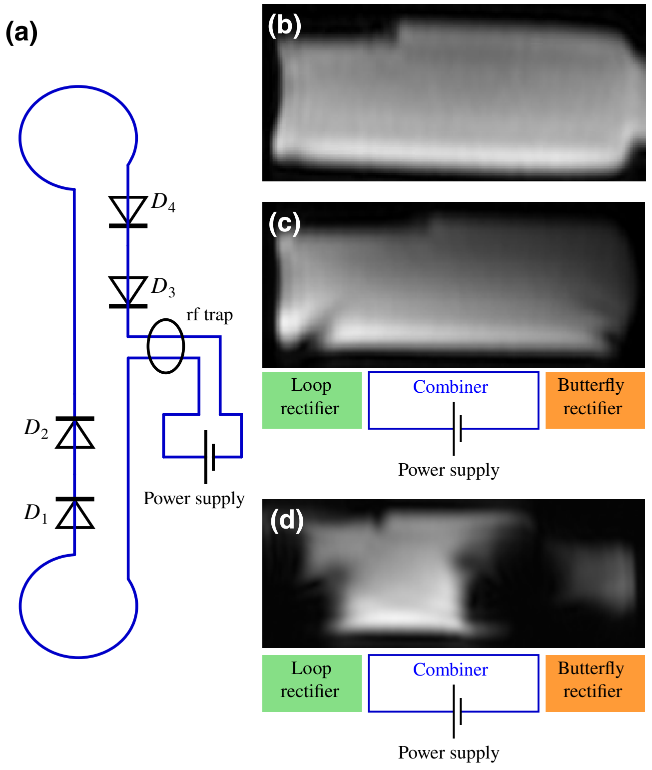

FIG. 7. (a) Schematics of the current loop emulating the dc circuitry of the combiner in Fig. 2. (b)–(d) Examples of magnetic resonance images for a phantom with or without an external dc current loop obtained with F2L sequence (image localizer, time repetition TR = 20 mS, echo time TE = 5.49 mS, field of view FOV = 300 mm, resolution 256 × 256). The loop at the bottom (blue solid line) emulates dc currents in the harvesting setup in a controllable fashion by the externally injected current I. (b) MR image of the phantom without any additional current sources attached ($I = 0$ mA). (c) MR image of the phantom in the presence of the dc current $I = 200$ mA in the wire loop (d) MR image of the phantom in the presence of the dc current $I = 1000$ mA in the wire loop.

measurements of the static magnetic field using magnetometer TD8620. The current loop is placed at a distance 1 cm from the high-resolution wrist coil phantom manufactured by the MRI Devices Corporation composed of $0,79$ g NaCl + $0,35$ g ($CuSO_4 - 5H_2O$) + 175 mL H_2O. The dimensions of the phantom are $42 \times 42 \times 150$ mm^3.

Figure 7(b) shows a reference MR image corresponding to zero current in the coil. The MR images obtained for nonzero currents in the coil are demonstrated in Figs. 7(c) and 7(d), respectively.

As seen in Fig. 7(c), the current $I = 200$ mA in the coil emulating the combiner dc loop readily yields recognizable distortions in the vicinity of the phantom. When the current reaches 1000 mA, the MR images become significantly distorted, Fig. 7(d). To eliminate this effect, one needs to minimize the generation of constant magnetic fields in the harvesting setup. This can be achieved via using differential wires in dc current loops and placing them as far as possible from the scanned object. Thus, one should perform careful analysis of such constant magnetic fields when developing practical harvesting solutions, and optimize the design of harvesting setup accordingly.

APPENDIX C: HARVESTED VOLTAGE FOR DIFFERENT PULSE SEQUENCES

The harvested power depends significantly on the type of MR pulse sequence. Since several parameters can be adjusted within each pulse sequence, we consider the most relevant ones in Table I. For example, it is seen that the harvesting voltage for FL2D (flash two-dimensional) pulse sequence is small because of the low power within a MRI scan, i.e., low FA and a single pulse used for excitation. However, for pulse sequences such as T2 TSE (turbo spin echo) the harvesting works better because of the higher single pulse power, several pulses in the excitation phase, and low TR (the time between consequent excitation pulses, or repetition time). The average power is estimated as the area under the slope of the voltage function with the help of a trapezoidal method, see Note S2 within the Supplemental Material [27].

TABLE I. Peak P_{peak} and average P_{av} harvested power, time repetition (TR), echo time (TE), and default flip angle (FA) for various pulse sequences (characterized by a different number of rf pulses within one working cycle) at the manual adjustment voltage $V_{\text{adj}} = 180$ V in the case of a 500-ohm load resistor.

Image sequence	No. of rf pulses	FA (°)	TR (ms)	TE (ms)	P_{peak} (mW)	P_{av} (mW)
FL2D	1	20	1500	200	242	60
T1 TSE	4	150	570	100	20808	400
T2 haste	3	150	2000	258	4050	180
T1 tirm	6	150	3500	30	21218	300
Diffusion	4	60	1800	106	19928	360

[1] Lena Nohava, Jean-Christophe Ginefri, Georges Willoquet, Elmar Laistler, and Roberta Frass-Kriegl, Perspectives in wireless radio frequency coil development for magnetic resonance imaging, Front. Phys. **8**, 11 (2020).

[2] Aasrith Ganti, Tracy Wynn, and Jenshan Lin, A novel energy harvesting circuit for rf surface coils in the mri system, IEEE Trans. Biomed. Circuits Syst. **15**, 791 (2021).

[3] Jens Höfflin, Elmar Fischer, Jürgen Hennig, and Jan G. Korvink, in *Proceedings of the International Society for Magnetic Resonance in Medicine*, Vol. 21 (2013), p. 728.

[4] Viacheslav Ivanov, Alena Shchelokova, Anna Andreychenko, and Alexey Slobozhanyuk, Coupled very-high permittivity dielectric resonators for clinical MRI, Appl. Phys. Lett. **117**, 103701 (2020).

[5] Kelly Byron, Fraser Robb, Pascal Stang, Shreyas Vasanawala, John Pauly, and Greig Scott, An RF-gated wireless power transfer system for wireless MRI receive arrays, Concepts Magn. Reson. Part B: Magn. Reson. Eng. **47B**, e21360 (2017).

[6] Mingzhao Song, Pavel Smirnov, Ekaterina Puhtina, Esmaeel Zanganeh, Stanislav Glybovski, Pavel Belov, and Polina Kapitanova, Multi-mode metamaterial-inspired resonator for near-field wireless power transfer, Appl. Phys. Lett. **117**, 083501 (2020).

[7] Kelly Byron, Chris Ellenor, Fraser Robb, Shreyas Vasanawala, John Pauly, and Greig Scott, in *Proceedings of the 22nd Annual Meeting of ISMRM*, Vol. 925 (2014).

[8] Kelly Byron, Simone A. Winkler, Fraser Robb, Shreyas Vasanawala, John Pauly, and Greig Scott, An MRI compatible RF MEMs controlled wireless power transfer system, IEEE Trans. Microw. Theory Tech. **67**, 1717 (2019).

[9] Aasrith Ganti, Jenshan Lin, Tracy Wynn, and Timothy Ortiz, Achieving electromagnetic compatibility of wireless power transfer antennas inside MRI system, Wireless Power Transfer **6**, 138 (2019).

[10] Mingzhao Song, Ivan Iorsh, Polina Kapitanova, Elizaveta Nenasheva, and Pavel Belov, Wireless power transfer based on magnetic quadrupole coupling in dielectric resonators, Appl. Phys. Lett. **108**, 023902 (2016).

[11] Mingzhao Song, Pavel Belov, and Polina Kapitanova, Wireless power transfer based on dielectric resonators with colossal permittivity, Appl. Phys. Lett. **109**, 223902 (2016).

[12] F. Cottone, H. Vocca, and L. Gammaitoni, Nonlinear Energy Harvesting, Phys. Rev. Lett. **102**, 080601 (2009).

[13] Mehmet Bakir, Muharrem Karaaslan, Olcay Altintas, Mehmet Bagmanci, Volkan Akdogan, and Feyzullah Temurtas, Tunable energy harvesting on UHF bands especially for GSM frequencies, Int. J. Microwave Wireless Technol. **10**, 67 (2017).

[14] Triet Le, Karti Mayaram, and Terri Fiez, Efficient far-field radio frequency energy harvesting for passively powered sensor networks, IEEE J. Solid-State Circuits **43**, 1287 (2008).

[15] Xiaolin Hu, Kamal Aggarwal, Mimi X. Yang, Kokab B. Parizi, Xiaoqing Xu, Demir Akin, Ada S. Y. Poon, and H.-S. Philip Wong, Micrometer-Scale Magnetic-Resonance-Coupled Radio-Frequency Identification and Transceivers for Wireless Sensors in Cells, Phys. Rev. Appl. **8**, 014031 (2017).

[16] Raghav Sharma, Rahul Mishra, Tung Ngo, Yong-Xin Guo, Shunsuke Fukami, Hideo Sato, Hideo Ohno, and

Hyunsoo Yang, Electrically connected spin-torque oscillators array for 2.4 GHz WiFi band transmission and energy harvesting, Nat. Commun. **12**, 1 (2021).

[17] Valentina Palazzi, Jimmy Hester, Jo Bito, Federico Alimenti, Christos Kalialakis, Ana Collado, Paolo Mezzanotte, Apostolos Georgiadis, Luca Roselli, and Manos M. Tentzeris, A novel ultra-lightweight multiband rectenna on paper for RF energy harvesting in the next generation LTE bands, IEEE Trans. Microw. Theory Tech. **66**, 366 (2018).

[18] Long Li Xuanming Zhang, Chaoyun Song, and Yi Huang, Progress, challenges, and perspective on metasurfaces for ambient radio frequency energy harvesting, Appl. Phys. Lett. **116**, 060501 (2020).

[19] Manuel Piñuela, Paul D. Mitcheson, and Stepan Lucyszyn, Ambient RF energy harvesting in urban and semi-urban environments, IEEE. Trans. Microw. Theory Tech. **61**, 2715 (2013).

[20] Robert W. Brown, Yu-Chung N. Cheng, E. Mark Haacke, Michael R. Thompson, and Ramesh Venkatesan, Magnetic Resonance Imaging: Physical Principles and Sequence Design (Second ed.) Wiley Blackwell, New Jersey, 2014.

[21] Mathias Blasche, Gradient performance and gradient amplifier power, Magnetom Flash **69**, 244 (2017).

[22] Bernhard Gruber, Martijn Froeling, Tim Leiner, and Dennis W. J. Klomp, RF coils: A practical guide for nonphysicists, J. Magn. Reson. Imaging **48**, 590 (2018).

[23] J. Thomas Vaughan, Carl J. Snyder, Lance J. DelaBarre, Patrick J. Bolan, Jinfeng Tian, Lizann Bolinger, Gregor Adriany, Peter Andersen, John Strupp, and Kamil Ugurbil, Whole-body imaging at 7T: Preliminary results, Magn. Reson. Med. **61**, 244 (2009).

[24] CPC Amps, Inc., *Introduction to NMR/MRI RF Amplifiers* (http://www.cpcamps.com/introduction-to-nmr-mri-amplifiers.html, 2012).

[25] Siemens, *Operator Manual Magnetom Prisma*, Vol. 1 (https://www.siemens-healthineers.com/, 2018).

[26] M. J. Riffe, J. A. Heilman, and M. A. Griswold, in *Proc. Intl. Soc. Mag. Reson. Med*, Vol. 15 (2007), p. 3273.

[27] See Supplemental Material at http://link.aps.org/supplemental/10.1103/PhysRevApplied.17.044014 for (i) the comparison of different considered designs of the harvesting coil; (ii) measurements of the signal waveforms for different MRI scanning sequences; (iii) details of numerical simulations in CST Microwave Studio.

[28] Michael Twieg, Michael A. de Rooij, and Mark A. Griswold, Active detuning of MRI receive coils with GaN FETs, IEEE Trans. Microw. Theory Tech. **63**, 4169 (2015).

[29] Steven W. Ellingson, *Electromagnetics* Vol. 1 (VT Publishing, Blacksburg, USA, 2018).

[30] Surajit Das Barman, Ahmed Wasif Reza, Narendra Kumar, Md. Ershadul Karim, and Abu Bakar Munir, Wireless powering by magnetic resonant coupling: Recent trends in wireless power transfer system and its applications, Renewable Sustainable Energy Rev. **51**, 1525 (2015).

[31] E. K. Insko and L. Bolinger, Mapping of the radiofrequency field, J. Magn. Reson., Ser. A **103**, 82 (1993).

[32] Matt A. Bernstein, Kevin F. King, and Xiaohong Joe Zhou, *Handbook of MRI Pulse Sequences* (Elsevier, Amsterdam, Netherlands, 2004).

[33] Ute Ludwig, Anne-Katrin Eisenbeiss, Christian Scheifele, Katja Nelson, Michael Bock, Jürgen Hennig, Dominik Von Elverfeldt, Olga Herdt, Tabea Flügge, and Jan-Bernd Hövener, Dental MRI using wireless intraoral coils, Sci. Rep. **6**, 1 (2016).

[34] Mirza Mansoor Baig, Hamid Gholamhosseini, and Martin J. Connolly, A comprehensive survey of wearable and wireless ECG monitoring systems for older adults, Med. Biol. Eng. Comput. **51**, 485 (2013).